

HelixTrack: Event-Based Tracking and RPM Estimation of Propeller-like Objects

Radim Spetlik Michal Pliska Vojtěch Vrba Jiri Matas
Faculty of Electrical Engineering
Czech Technical University in Prague

Abstract

Safety-critical perception for unmanned aerial vehicles and rotating machinery requires microsecond-latency tracking of fast, periodic motion under egomotion and strong distractors. Frame- and event-based trackers drift or break on propellers because periodic signatures violate their smooth-motion assumptions. We tackle this gap with HelixTrack, a fully event-driven method that jointly tracks propeller-like objects and estimates their rotations per minute (RPM). Incoming events are back-warped from the image plane into the rotor plane via a homography estimated on the fly. A Kalman Filter maintains instantaneous estimates of phase. Batched iterative updates refine the object pose by coupling phase residuals to geometry. To our knowledge, no public dataset targets joint tracking and RPM estimation of propeller-like objects. We therefore introduce the Timestamped Quadcopter with Egomotion (TQE) dataset with 13 high-resolution event sequences, containing 52 rotating objects in total, captured at distances of 2 m/4 m, with increasing egomotion and microsecond RPM ground truth. On TQE, HelixTrack processes full-rate events $\approx 11.8\times$ faster than real time and microsecond latency. It consistently outperforms per-event and aggregation-based baselines adapted for RPM estimation.

1. Introduction

Tracking propellers and reading their instantaneous RPM is a practical capability for working with and around small aerial vehicles. In radio-denied or silent settings, blade phase and RPM provide a communication-free signal for leader-follower behavior, intent (spool-up/spool-down), and collision avoidance, and act as a diagnostic or identification cue when other channels fail. However, fast rotors produce dense, strictly periodic patterns and visually similar distractors that violate the motion assumptions of conventional frame-based and event-based trackers, motivating an event-native, propeller-aware solution.

In recent years, event-stream tracking has attracted in-

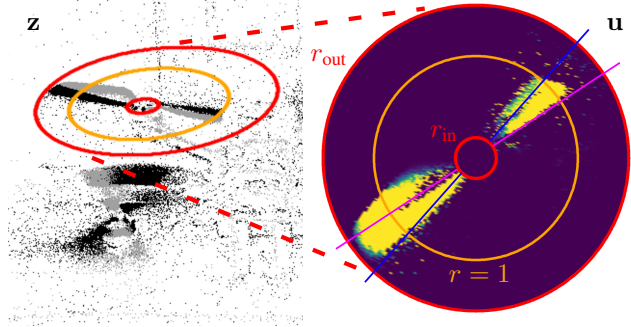


Figure 1. *HelixTrack* – tracking and instantaneous rotations per minute estimation of propeller-like objects from asynchronous events. Incoming events are back-warped from the image plane “z” into the rotor plane “u” by a homography. Rotor-plane coordinates are gated with r_{in} and r_{out} to a ring-shaped band and used for: (i) per-event phase update via Kalman filter, and (ii) batched pose refinement via iterative homography update.

creasing attention, with research advancing from feature-level tracking to single- and multi-object tracking, supported by new datasets and strong baselines [3, 4, 10, 12–14]. Two families of approaches have proven particularly effective. *Per-event* methods process each event as it arrives and update the state continuously, yielding very low latency and strong robustness in high-speed regimes [15, 16]. Examples include asynchronous continuous optimization over event constellations [16] and Kalman-filtered blob tracking that embraces native, event-driven timing [15]. *Aggregation-based* methods store events in spatiotemporal tensors — event frames, time surfaces, or voxel grids — which can be processed by modern deep networks and sequence models [10, 12–14]. Such aggregation enables the use of powerful learned backbones (e.g., transformers and state-space models) which have delivered competitive accuracy across single- and multi-object tracking benchmarks [10, 12–14]. Thus, both paradigms have established themselves as viable choices for event-based tracking, trading off latency, modeling flexibility, and learning capacity.

However, an important set of phenomena remains under-explored: objects that exhibit fast, periodic mo-

tion. Rotating propellers are archetypal: they generate dense, structured, highly periodic event patterns that violate the “smooth translational motion” assumptions implicit in many trackers. Rapid movement of blades, strong distractors (*e.g.*, in the case of multiple propellers), and repetitive textures challenge both per-event and aggregation-based object trackers, leading to drift and failures. Event-based rate estimation for periodic phenomena has been studied [2, 7], but prior work focused on estimating frequency in static scenes where no tracking is required. To our knowledge, no prior work explicitly formulates and solves the tracking of objects exhibiting periodic motion while jointly estimating their rotation rate (RPM) from raw events.

We address this gap with *HelixTrack*, an event-based framework for *propeller tracking and RPM estimation*. Our key insight is that a rotating blade induces a *helical signature* in the event space when lifted to appropriate spatiotemporal coordinates anchored on the rotor hub. *HelixTrack* is a *fully event-driven, real-time, low-latency* framework for tracking and measuring spinning propeller-like objects with an event camera (see Fig. 1). *HelixTrack*: (i) back-warps each event through a homography onto the rotor plane while applying various hard and soft gates, (ii) uses an Extended Kalman Filter (EKF) to estimate the instantaneous phase, angular speed, and acceleration, and (iii) iteratively updates the homography, minimizing a set of refined loss terms. The outcome is a stream of phase and pose updates from which RPM follows directly. Conceptually, *HelixTrack* bridges both families of prior work: it runs natively *asynchronously*, retaining the latency benefits of event cameras, yet its *lifted, structured representation* admits aggregation for frame- or batch-based pipelines.

We also overcome a common limitation of event-based tracking — the absence of reliable ground-truth positions. Annotating the trajectories of rapidly spinning propeller hubs observed by a moving camera presents significant challenges and requires substantial time investment. To address this, we introduce a dataset that provides microsecond-level accurate ground-truth RPM measurements for each propeller, enabling evaluation through the mean absolute error of the predicted RPM, which is a dependable indicator of the tracker’s precision.

Beyond drone propellers, the formulation is applicable to other periodic, radially symmetric actuators (*e.g.*, fans, rotors), offering a principled path to track-and-measure behaviors that are challenging for conventional trackers.

In summary, our contributions are:

- (i) **Problem formulation.** We specify the task and evaluation protocol for event-based tracking with joint RPM estimation of propeller-like objects exhibiting periodic, high-speed motion. This fits in-between the general event-based trackers [10, 12–16] and rate-only estimators that are not object-centric [2, 7].
- (ii) **The *HelixTrack* model.** We propose an event-driven tracker that back-warps events to the rotor plane via a homography, fits a helical phase model, and jointly infers RPM, with a per-event EKF, and pose, using the Gauss-Newton (GN) algorithm on event batches.
- (iii) **The *TQE Dataset*.** We collect 13 high-resolution sequences captured at 2 m / 4 m distances with seven ego-motion levels, and synchronized IR-RPM ground truth.
- (iv) **Benchmark.** We adapt asynchronous [15] and learned [4] trackers for RPM estimation and show that *HelixTrack* achieves the best performance.
- (v) **Ablations & Runtime analysis.** We ablate loss terms, test tolerance to coarse pose/scale/RPM initialization, and profile speed — processing at $\approx 11.8\times$ real time with accuracy/throughput trade-offs under subsampling. *HelixTrack* turns an adversarial motion pattern into a feature that can be modeled, localized, and measured.

2. Related Work

The review of *tracking* literature relevant to *HelixTrack* is organized by tracking paradigms and sensing modalities.

Event cameras natively support low-latency motion perception, which has motivated blob- and feature-level trackers as well as general single-object tracking (SOT) pipelines. Asynchronous blob trackers operate directly on the event stream, *i.e.* without frames, maintaining object hypotheses with simple motion and shape cues [3, 4, 15, 16]. At the feature level, data-driven formulations learn to follow high-speed structures through the spatio-temporal event volume, improving robustness over hand-crafted rules [3, 4]. Benchmarks for event-based visual object tracking (VOT) enable comparison across VOT methods [13, 14].

Tracking-by-detection and joint detection-tracking have also been explored in the event domain. Recent work demonstrates end-to-end multi-object tracking on events with learned association and sparsity-aware motion models [12]. Beyond local heuristics, sequence models capture long-range temporal dependencies in asynchronous data. State-space models and transformer-style architectures have been adapted to event streams for VOT, producing stronger appearance modeling under severe motion and illumination change [10, 14]. Several approaches fuse events with intensity frames (or other modalities) to reduce failure modes of either sensor alone, typically with transformer-based fusion and hybrid feature pipelines [10]. In contrast, our method is *fully event-driven*, which preserves very low latency.

Event cameras have also been used for geometry-aware tracking — *e.g.*, 3D feature trajectories and object-grounded motion constraints — which is particularly relevant when the target exhibits structured dynamics [3]. Our formulation continues this line by embedding a physics/geometry prior in the tracker state.

An orthogonal thread optimizes a continuous-time ob-

jective directly over events for tracking and registration, offering drift control and accurate sub-frame localization [16]. We instead cast tracking as online filtering with an explicit dynamical phase model, which trades some global optimality for latency and simplicity.

Previous unmanned aerial vehicle (UAV) tracking work has focused on estimating drone position or pose rather than measuring propeller attributes. Frame-based methods often rely on standard cameras and CNN-based pipelines [11, 17, 18], providing velocities and accelerations with significant latency. Event-based techniques for high-speed UAV interception or localization [5, 6, 8, 9] sometimes detect propeller patterns in real time at modest rates (e.g., 35 Hz [6]). However, they rarely localize individual propellers or measure angular velocity at microsecond temporal precision, and typically leverage low-resolution sensors, hampering performance in cluttered scenes or for small targets. In [1] propeller speeds are measured but no tracking is performed. **Relation to our work.** Unlike detection-oriented pipelines that classify or localize events on a per-frame basis, our tracker maintains the *phase and pose* of a specific object continuously over time, using only asynchronous events.

3. Method

High-level summary. Given an approximate pose and RPM from [7], the tracker estimates two coupled quantities: (i) an image-to-rotor-plane homography (geometry), and (ii) a latent phase state $\mathbf{x}(t) = [\phi(t), \omega(t), \alpha(t)]^\top$ (phase and its first and second derivatives). Asynchronously arriving events are processed in two loops:

1. **Per-event phase tracking.** An EKF updates $\mathbf{x}(t)$ from each event using a wrapped phase residual.
2. **Batched pose refinement.** Periodically, Gauss-Newton (GN) updates homography parameters by minimizing a robust, weighted objective with analytic Jacobians.

The EKF gives microsecond-scale phase and RPM tracking, while GN accumulates evidence to estimate pose.

3.1. Problem Setup and Notation

Camera observes an event stream $e_i = (\mathbf{z}_i, t_i, p_i)$ with pixel location $\mathbf{z}_i = (x_i, y_i)^\top$, timestamp t_i , and polarity $p_i \in \{+1, -1\}$. Vectors are bold; we reserve \mathbf{x} for the phase state and \mathbf{z} for image points.

Homography parameterization (image \leftrightarrow rotor plane). A planar point $\mathbf{u} = (u_x, u_y)^\top$ in the rotor plane projects to the image via a 6-DoF homography

$$\mathbf{H}(\mathbf{q}) = \begin{bmatrix} s \cos \psi & -s \sin \psi & t_x \\ s \sin \psi & s \cos \psi & t_y \\ p_{31} & p_{32} & 1 \end{bmatrix} \quad (1)$$

$$\mathbf{z} \sim \mathbf{H}(\mathbf{q}) [\mathbf{u}; 1], \quad \mathbf{q} = [s, \psi, t_x, t_y, p_{31}, p_{32}]^\top, \quad (2)$$

where $s > 0$ (in-plane scale), ψ (in-plane rotation), (t_x, t_y) (translation), and (p_{31}, p_{32}) (small perspective terms). Given an event location \mathbf{z}_i ,

$$\tilde{\mathbf{u}}_i = \mathbf{H}(\mathbf{q})^{-1}[\mathbf{z}_i; 1], \quad \mathbf{u}_i = \frac{1}{\tilde{u}_{i,3}} \begin{bmatrix} \tilde{u}_{i,1} \\ \tilde{u}_{i,2} \end{bmatrix}, \quad \frac{\partial \mathbf{u}_i}{\partial \mathbf{q}} \in \mathbb{R}^{2 \times 6}.$$

3.2. Generative Phase Model

We map each event to a common phase coordinate that is invariant to arbitrary in-plane camera rotation and respects the B -fold symmetry of a B -blade rotor. Let $\zeta \in \{\pm 1\}$ be the *rotation sign*, estimated from circular statistics over a short prefix of events. The signed azimuth is

$$\theta_\zeta(\mathbf{u}) = \text{atan2}(\zeta u_y, u_x) \in (-\pi, \pi].$$

To absorb the image-plane rotation ψ (2) into the rotor phase $\phi(t)$ (radians), we define the effective phase

$$\phi_{\text{eff}}(t) = \phi(t) - B\psi.$$

ϕ_{eff} is the tracked phase after accounting for ψ . Given the timestep t_i and the back-wrapped position \mathbf{u}_i of an event e_i , we form the wrapped *phase residual*

$$\varepsilon_i^\phi = \text{wrap}_\pi(\phi_{\text{eff}}(t_i) - B\theta_\zeta(\mathbf{u}_i)). \quad (3)$$

where $\text{wrap}_\pi(\theta) = \text{mod}(\theta + \pi, 2\pi) - \pi$. By construction, ε_i^ϕ is the π -wrapped, signed phase error between $\phi_{\text{eff}}(t_i)$ and the blade phase implied by the event, $B\theta_\zeta(\mathbf{u}_i)$. Ignoring wrap discontinuities, the residual is first-order invariant to global in-plane rotation:

$$\frac{\partial \varepsilon_i^\phi}{\partial \psi} = \frac{\partial \phi_{\text{eff}}}{\partial \psi} - B \frac{\partial \theta_\zeta}{\partial \psi} = -B - B(-1) = 0,$$

since a global rotation shifts all azimuths by $-\psi$ so that $\partial \theta_\zeta / \partial \psi = -1$.

3.3. Phase-State Dynamics: Constant Acceleration with White Jerk

We want to stay predictive between irregular event times. We therefore use a continuous-time acceleration prior whose uncertainty grows with elapsed time. Note that t, t' are continuous. By definition of angular kinematics,

$$\omega(t) = \dot{\phi}(t), \quad \alpha(t) = \dot{\omega}(t) = \ddot{\phi}(t), \quad j(t) = \dot{\alpha}(t) = \dddot{\phi}(t),$$

units ω [rad/s], α [rad/s²], j [rad/s³]. We model $j(t)$ as “white jerk”, *i.e.*, zero-mean white Gaussian noise with spectral density q_{jerk} , *i.e.* $\mathbb{E}[j(t)j(t')] = q_{\text{jerk}}\delta(t - t')$, capturing torque fluctuations giving the continuous-time SDE

$$\dot{\mathbf{x}}(t) = \mathbf{A} \mathbf{x}(t) + \mathbf{L} w(t), \quad w(t) \sim \mathcal{N}(0, q_{\text{jerk}}\delta(t - t')),$$

$$\mathbf{A} = \begin{bmatrix} 0 & 1 & 0 \\ 0 & 0 & 1 \\ 0 & 0 & 0 \end{bmatrix}, \quad \mathbf{L} = \begin{bmatrix} 0 \\ 0 \\ 1 \end{bmatrix}.$$

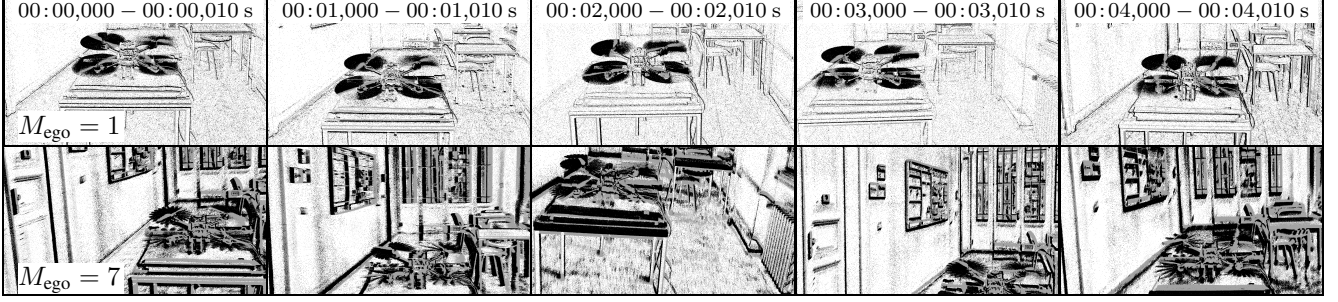


Figure 2. Aggregated events from two sequences in the Timestamped Quadcopter with Egomotion dataset. Top row: smallest egomotion ($M_{\text{ego}} = 1$); bottom row: largest egomotion ($M_{\text{ego}} = 7$). Events are aggregated from the first 10 ms of five 1-second intervals.

Using $\mathbb{E}[j(t)j(t')] = q_{\text{jerk}}\delta(t-t')$ and integrating the process noise through the continuous-time model yields $\mathbf{Q}_d(\Delta t_i) = \int_0^{\Delta t_i} [\frac{\tau^2}{2}, \tau, 1] q_{\text{jerk}} [\frac{\tau^2}{2}, \tau, 1]^\top d\tau$, $\Delta t_i = t_i - t_{i-1}$, evaluating to

$$\mathbf{Q}_d = q_{\text{jerk}} \begin{bmatrix} \frac{\Delta t_i^5}{20} & \frac{\Delta t_i^4}{8} & \frac{\Delta t_i^3}{6} \\ \frac{\Delta t_i^4}{8} & \frac{\Delta t_i^3}{3} & \frac{\Delta t_i^2}{2} \\ \frac{\Delta t_i^3}{6} & \frac{\Delta t_i^2}{2} & \Delta t_i \end{bmatrix}.$$

We discretize the continuous-time state by the event times t_i . Thus, \mathbf{x}_{i-1} is the state immediately *after* assimilating event e_{i-1} . It is propagated over Δt_i to form

$$\mathbf{x}_i = \mathbf{F}(\Delta t_i) \mathbf{x}_{i-1},$$

$$\mathbf{P}_i = \mathbf{F}(\Delta t_i) \mathbf{P}_{i-1} \mathbf{F}(\Delta t_i)^\top + \mathbf{Q}_d(\Delta t_i),$$

$$\mathbf{F} = \exp(\mathbf{A}\Delta t_i) = \begin{bmatrix} 1 & \Delta t_i & \frac{1}{2}\Delta t_i^2 \\ 0 & 1 & \Delta t_i \\ 0 & 0 & 1 \end{bmatrix}.$$

3.4. Extended Kalman Filter Update

We gate events by a von Mises window $w_{\text{vm}}(\varepsilon^\phi) = \exp\{\kappa(\cos(\varepsilon^\phi) - 1)\}$, where κ controls angular selectivity ($\kappa = 0$ means no gating). We make the innovation variance heteroscedastic using the gates:

$$R_i = \frac{\sigma_0^2}{\max\{w_{\text{vm}}(\varepsilon_i^\phi) w_{\text{ring}}(r_i; \sigma_{\text{ring}}), \epsilon\}},$$

where σ_0^2 is a nominal phase noise, ε_i^ϕ is the phase residual (3), and $\epsilon > 0$ prevents division by zero. A smooth spatial gate emphasizes the blade-tip neighborhood (normalized near $r = 1$):

$$w_{\text{ring}}(r; \sigma_{\text{ring}}) = \exp\left[-\frac{1}{2}\left(\frac{r-1}{\sigma_{\text{ring}}}\right)^2\right].$$

The event e_i yields the EKF update

$$\mathbf{K}_i = \mathbf{P}_i \mathbf{C}^\top (\mathbf{C} \mathbf{P}_i \mathbf{C}^\top + R_i)^{-1},$$

$$\mathbf{x}_i \leftarrow \mathbf{x}_i - \mathbf{K}_i \varepsilon_i^\phi, \quad \mathbf{P}_i \leftarrow (\mathbf{I} - \mathbf{K}_i \mathbf{C}) \mathbf{P}_i,$$

where $\mathbf{C} = [1 \ 0 \ 0]$.

3.5. Gauss-Newton Pose Refinement

We refine \mathbf{q} on mini-batches of events $\mathcal{B} \subset \{1, \dots, N\}$ using GN with analytic Jacobians. Let $r_i = \|\mathbf{u}_i\|$. In addition to phase residual ε_i^ϕ , we define the *radial residual*

$$\varepsilon_i^r = r_i - 1,$$

which pushes the average radius of projected events to the unit radius $r = 1$.

Next, we add the *polarity residual*

$$\varepsilon_i^{\text{pol}} = c_{\text{pol}} \sin\left(\frac{1}{2} \text{wrap}_\pi(\varepsilon_i^\phi - \theta_{\text{pol}}(p))\right),$$

to align the event polarity p with the expected edge phase. $\theta_{\text{pol}}(+)$ = c_+ , $\theta_{\text{pol}}(-)$ = c_- , and c_{pol} are constants.

We focus on an informative annulus $r_{\text{in}} \leq r_i \leq r_{\text{out}}$ (see Fig. 1) and incorporate *soft annulus residuals*

$$\varepsilon_i^{\text{in}} = c_b \text{softplus}_\tau(r_{\text{in}} - r_i), \quad \varepsilon_i^{\text{out}} = c_b \text{softplus}_\tau(r_i - r_{\text{out}}),$$

with $\text{softplus}_\tau(s) = \tau \log(1 + e^{s/\tau})$, ($\tau > 0$), and $c_b \in \mathbb{R}$ is a constant.

Since scale and perspective can drift when more events fall just *outside* than *inside* the expected tip radius, we add the Balanced Tip Occupancy (BTO) regularizer that encourages a balanced fraction of events around the unit radius $r=1$. We accumulate the event counts C_{core} , C_{in} , and C_{out} , which are the numbers of events in three narrow radial bands around the tip — core at $r = 1$, inside at $1 - \Delta$, and outside at $1 + \Delta$. Rate-invariant inside/outside fractions are

$$p_{\text{in}} = \frac{C_{\text{in}}}{C_{\text{core}} + \epsilon}, \quad p_{\text{out}} = \frac{C_{\text{out}}}{C_{\text{core}} + \epsilon},$$

with $\epsilon > 0$. The *BTO penalty* is

$$\ell_{\text{BTO}} = \text{softplus}_\tau(p_{\text{out}} - \bar{p}_{\text{out}}) + \text{softplus}_\tau(\bar{p}_{\text{in}} - p_{\text{in}}),$$

\bar{p}_{out} and \bar{p}_{in} are constants. Gradients flow through the radial channel, stabilizing scale and perspective at the blade tips.

Objective function for pose estimation. Let $\rho_2(s) = \frac{1}{2}s^2$ and define event gates $g_i^\phi = \lambda_\phi w_i^\phi$, $g_i^r = \lambda_r w_i^r$ with

$$w_i^\bullet = w_{\text{vm}}(\varepsilon_i^\phi) w_{\text{ring}}(r_i; \sigma_{\text{ring}}) w_{\text{Huber}}(\varepsilon_i^\bullet; \mathbf{c}_\bullet), \quad \bullet \in \{\phi, r\},$$

where $w_{\text{Huber}}(\varepsilon; c) = \min\{1, c/|\varepsilon|\}$ with threshold $c > 0$. The batch objective is

$$\begin{aligned} \mathcal{L}(\mathbf{q}) = & \sum_{i \in \mathcal{B}} \left[g_i^\phi \rho_2(\varepsilon_i^\phi) + g_i^r \rho_2(\varepsilon_i^r) \right] \\ & + \lambda_{\text{pol}} \sum_{i \in \mathcal{B}} \rho_2(\varepsilon_i^{\text{pol}}) + \lambda_{\text{band}} \left(\sum_{i \in \mathcal{B}} \rho_2(\varepsilon_i^{\text{in}}) + \sum_{i \in \mathcal{B}} \rho_2(\varepsilon_i^{\text{out}}) \right) \\ & + \lambda_{\text{BTO}} \ell_{\text{BTO}}(p_{\text{in}}, p_{\text{out}}) + \lambda_{\text{reg}} \ell_{\text{reg}}(\mathbf{q}). \end{aligned} \quad (4)$$

Interpretation. The first line ties phase to geometry (via ε_i^ϕ) and centers the working ring at $r=1$ (via ε_i^r). The gates w_{vm} and w_{ring} downweight azimuthally inconsistent or off-band events, and w_{Huber} reduces heavy-tailed outliers. The second line adds weak supervision (polarity alignment, soft band barriers). BTO inhibits degenerate “only-inside” or “only-outside” fits. Finally, ℓ_{reg} regularizes weakly observable directions (e.g., $\|p_{31}\|^2 + \|p_{32}\|^2$). We choose $\lambda_\phi \approx 1/\sigma_\phi^2$ and $\lambda_r \approx 1/\sigma_r^2$, and set Huber thresholds c_ϕ, c_r at $1 \sim 2$ standard deviations.

GN system and update. Linearizing the residuals in (4) yields normal equations that we omit from the main paper for brevity (see supplementary Sec. S1 for the full system). We solve the equations in the least-square sense with Gauss-Newton algorithm and update

$$\mathbf{q} \leftarrow \mathbf{q} + \Gamma \Delta \mathbf{q}, \quad \Gamma = \text{diag}(\gamma_{\text{scale}}, \gamma_{\text{rot}}, \gamma_{\text{tx}}, \gamma_{\text{ty}}, \gamma_{\text{persp}}, \gamma_{\text{persp}}),$$

where Γ sets the update step size for each homography parameter. A pose update is triggered if $|\langle \phi - \phi_{\text{base}} - B(\psi - \psi_{\text{base}}) \rangle / B| \geq \pi$, defining the latency of the pose estimation. Note that gradient descent in the direction of $\mathcal{L}(\mathbf{q})$ minimization is also possible, in this small 6-DoF least-squares tracker, Gauss-Newton is preferable. It exploits the residual/Jacobian structure to take curvature-aware, parameter-coupled steps.

3.6. RPM Estimation

Instantaneous angular speed and RPM are

$$\hat{\omega} = |\dot{\omega}|, \quad \widehat{\text{RPM}} = \frac{60}{2\pi} \hat{\omega}, \quad \text{RPM}_{\text{shaft}} = \widehat{\text{RPM}}/B,$$

since $\omega = \dot{\phi}$.

Implementation Details We process events sequentially:

1. **Predict** $(\mathbf{x}_i, \mathbf{P}_i)$ with $(\mathbf{F}, \mathbf{Q}_d)$.
2. **Update EKF** with ε_i^ϕ using gates $w_{\text{vm}}, w_{\text{ring}}$.
3. **Accumulate GN terms** using analytic $\partial \mathbf{u} / \partial \mathbf{q}$.
4. **Pose step** Apply a batched GN update when triggered.

Assumptions. (i) A single planar homography adequately models the rotor; (ii) the helical phase model is accurate within the informative ring.

4. Experiments

We first introduce the newly collected Timestamped Quadcopter with Egomotion (TQE) dataset, then detail the evaluation protocol and metrics, and finally present experiments. Unless otherwise specified, results are reported using 4-fold cross-validation over the four propellers in TQE recordings (one training propeller per fold).

4.1. Dataset

Timestamped Quadcopter with Egomotion (TQE) dataset contains 13 sequences of a quadcopter with four propellers, recorded at distances of 2 and 4 meters, containing 52 rotating objects in total. Sequences are captured with Metavision EVK4HD event camera. Each sequence shows the quadcopter moving progressively faster, starting with near-hovering to mimic light wind and progressing to rapid, shaky movements similar to drone racing. The level of egomotion of the camera is indicated by $M_{\text{ego}} \in \{1, \dots, 7\}$, where higher values represent a greater intensity of motion (see Fig. 2). Camera settings, such as aperture and focus, were tuned for varying distances. The Arduino-regulated propeller speeds were calibrated to a spiral path, simulating real flight, with motor speeds ranging from 30-80% of maximum. An infrared sensor aimed at reflective tape on the rotor measured the values, with its analog output passed to the camera’s trigger input. In all recordings, the quadcopter is mounted on a table and the camera is held in hand.

4.2. Accuracy metrics

We evaluate a tracker by the mean absolute error (MAE), mean absolute relative error (MArE), and root mean squared error (RMSE) between its instantaneous shaft speed and the infrared (IR) sensor ground truth. The tracker internally estimates angular speed ($\omega(t)$) (Sec. 3.6), and we convert it to RPM and to shaft RPM. The IR setup produces time-synchronized, microsecond-accurate shaft-speed measurements for each propeller (the comparator output is synchronized with the camera clock), which we treat as the ground truth ($\text{RPM}_{\text{GT}}(t)$). We compute the per-sequence errors as

$$\text{MAE}_{\text{seq}} = \frac{1}{|\mathcal{T}|} \sum_{t \in \mathcal{T}} \left| \widehat{\text{RPM}}_{\text{shaft}}(t) - \text{RPM}_{\text{GT}}(t) \right|,$$

$$\text{MArE}_{\text{seq}} = \frac{1}{|\mathcal{T}|} \sum_{t \in \mathcal{T}} \frac{\left| \widehat{\text{RPM}}_{\text{shaft}}(t) - \text{RPM}_{\text{GT}}(t) \right|}{\left| \text{RPM}_{\text{GT}}(t) \right|},$$

$$\text{RMSE}_{\text{seq}} = \sqrt{\frac{1}{|\mathcal{T}|} \sum_{t \in \mathcal{T}} \left(\widehat{\text{RPM}}_{\text{shaft}}(t) - \text{RPM}_{\text{GT}}(t) \right)^2},$$

where (\mathcal{T}) is the set of tracker update times (asynchronous for per-event methods, discrete for aggregation baselines). Unless stated otherwise, all results are reported as shaft RPM.

d	M_{ego}	l (s)	propeller	MAR \bar{E} (%) \downarrow			MAE (RPM) \downarrow			RMSE (RPM) \downarrow		
				ours	AEB [15]	DeepEv [4]	ours	AEB [15]	DeepEv [4]	ours	AEB [15]	DeepEv [4]
2 m	1	28.7	rear right	1.3	61.4	8564.8	93.7	5980.8	652423.7	215.9	7186.8	785896.2
			rear left	1.3	0.9	402.4	81.4	73.0	32090.3	241.4	241.2	46466.0
			front left	1.5	35.3	4132.0	118.4	2487.0	303141.3	194.1	3302.9	359054.3
			front right	1.2	65.5	94.6	77.8	5650.8	8759.2	186.3	7673.3	9700.4
	3	27.7	rear right	1.2	1198.7	5013.6	85.1	102482.5	386360.6	223.2	192935.8	437954.9
			rear left	31.7	15.0	2059.8	2137.8	1696.4	151319.8	4518.8	3482.9	184206.2
			front left	4.2	467.5	5236.2	230.2	37691.4	376231.1	763.8	81016.3	448776.7
			front right	4.8	1347.9	195.7	267.9	110056.2	14595.8	1031.9	202948.8	18910.5
	5	28.8	rear right	62.3	531.3	106.7	6347.2	41415.3	9244.0	7842.7	79321.0	10241.1
			rear left	100.9	480.0	117.9	9689.7	30491.9	10624.2	10899.5	67097.7	12239.0
			front left	65.0	389.8	99.3	5045.3	33458.3	8963.0	6266.7	69659.2	9836.3
			front right	97.7	1122.0	398.5	8871.4	77151.0	32523.2	9710.6	111267.4	56823.0
4 m	1	28.7	rear right	73.1	285.5	834.5	6616.3	21029.7	57801.3	8517.8	46759.1	73901.3
			rear left	1.2	57.2	89.6	76.4	6038.7	8341.9	158.4	20115.0	9422.8
			front left	1.4	48.9	88.7	104.8	4676.4	7853.7	255.3	16769.4	8925.9
			front right	1.3	165.4	835.4	87.8	13041.8	58054.3	319.4	36853.1	74833.5
	3	28.9	rear right	70.9	58.8	95.8	5770.0	5904.9	9773.3	7008.1	11479.0	10725.7
			rear left	1.3	46.8	1801.4	85.0	3960.0	140787.4	211.7	4845.4	181653.8
			front left	1.3	303.1	1937.2	109.4	21349.0	146814.9	210.8	51357.9	174482.0
			front right	79.8	39.7	97.4	7832.8	4091.3	9594.5	9394.6	5306.3	10465.4
	5	27.2	rear right	95.3	994.6	97.8	9688.6	83816.5	9942.3	10614.2	127547.1	10817.5
			rear left	93.9	1043.3	94.8	9316.3	76882.9	9332.0	10400.6	133235.2	10351.1
			front left	1.7	1092.8	3339.1	119.1	81598.8	260136.5	241.1	126119.1	310936.4
			front right	88.3	1126.9	95.6	8752.7	93336.6	9351.7	9711.9	134050.9	10281.2

Table 1. Benchmark on selected recordings of Timestamped Quadcopter with Egomotion (TQE). For each presented method and setting (camera-target distance d , egomotion level M_{ego}), the average shaft-RPM mean absolute relative error (MAR \bar{E}), mean absolute error (MAE), and root mean squared error (RMSE) are reported over 4-fold cross-validation across the four propellers (one training propeller per fold). Both AEB-Tracker [15] and DeepEv [4] methods were modified to allow RPM estimation (see Sec. 4.3). TQE ground-truth RPM has $\mu \pm \sigma = 11193 \pm 3540$, min 917, max 15768. Duration l of recording reported in seconds. $M_{\text{ego}} = 1$ roughly means “slow camera movement”, while $M_{\text{ego}} = 5$ means “fast camera movement” (see Fig. 2). As M_{ego} increases, the camera experiences stronger egomotion, leading to increase of the number of events generated in the background. Complete results are provided in supplementary Table S3.

4.3. Benchmarking against existing trackers

In our benchmarks, we include the asynchronous blob tracker [15] and the data-driven feature tracker [4] because they represent complementary, strong event-native baselines that map directly to rotor-RPM estimation with minimal changes. The tracker [15] operates purely asynchronously on raw events and tracks compact “event blobs”. In contrast, the deep tracker [4] produces high-rate point trajectories. Both methods have mature public implementations, are designed for fast, high-dynamic-range motion, and together bracket the model-based vs. learned design space, enabling comparisons with minimal adaptations to the propeller-tracking setting of RPM estimation. The next two sections detail these task-specific modifications.

4.3.1. AEB-Tracker modifications

We adapted the original event tracker [15] to rotor targets by (i) using an ellipse-aligned gate for event association and (ii) estimating RPM directly from the tracked ellipse orientation. Specifically, for an event at (c, r) and track i with

center (z_{x_i}, z_{y_i}) , semi-axes $(\lambda_{1,i}, \lambda_{2,i})$ and orientation θ_i , we compute the ellipse-frame residual

$$\begin{bmatrix} e_x \\ e_y \end{bmatrix} = \begin{bmatrix} \cos \theta_i & \sin \theta_i \\ -\sin \theta_i & \cos \theta_i \end{bmatrix} \begin{bmatrix} c - z_{x_i} \\ r - z_{y_i} \end{bmatrix},$$

$$d_i = \sqrt{\left(\frac{e_x}{\lambda_{1,i}}\right)^2 + \left(\frac{e_y}{\lambda_{2,i}}\right)^2},$$

and accept the event if $d_i < \tau$ (adaptive τ). This replaces the original Euclidean pixel gate, making the association geometry-aware for slender blades. We also initialize $(z_x, z_y, \lambda_1, \lambda_2)$ to match the rotor footprint.

RPM from orientation. The filter tracks the ellipse orientation $\theta(t) \in [0, \pi)$. We unwrap it with $\Delta\theta_k = \text{wrap}_{(-\pi/2, \pi/2]}(\theta_k - \theta_{k-1})$ and $\Phi_k = \Phi_{k-1} + \Delta\theta_k$. Whenever $|\Phi|$ increases by 2π between times t_1 and t_2 we update an instantaneous RPM estimate

$$\widehat{\text{RPM}} = \frac{B \cdot 60}{t_2 - t_1},$$

where the factor B compensates the π -periodicity of θ . Equivalently, $\widehat{\text{RPM}}(t) = \frac{60}{\pi} \dot{\theta}(t)$ using the unwrapped θ .

In addition to the task-specific changes described above, we tuned the tracker’s parameters one by one. After qualitatively confirming that this setup produced correct tracks for about 10 ms at the start of each sequence, we ran a grid search around these values (see supplementary Sec. S3).

4.3.2. DeepEv Tracker Modifications

Given DeepEv [4] tracklets $\mathcal{T} = \{(t_i, \mathbf{z}_i)\}_{i=1}^N$ with $\mathbf{z}_i = (z_{x_i}, z_{y_i})$, we adopt the same EKF used by HelixTrack for phase estimation and reuse the homography $\mathbf{H} \in \mathbb{R}^{3 \times 3}$ estimated by HelixTrack. To preserve the estimated perspective and scale while anchoring the warp to the DeepEv image-plane measurements, we overwrite the translation entries of H for each observation \mathbf{z}_i :

$$\mathbf{H}_{13} \leftarrow z_{x_i} \mathbf{H}_{33}, \quad (5)$$

$$\mathbf{H}_{23} \leftarrow z_{y_i} \mathbf{H}_{33}. \quad (6)$$

This keeps the projective scale \mathbf{H}_{33} fixed and injects the DeepEv positions into the homography. Our rationale is that, even when our homography estimate degrades in some recordings, accurate DeepEv tracklets should produce results comparable to those of HelixTrack.

We could not fine-tune the model (no ground-truth tracks or camera poses are available), and we could not modify the method due to its deep network nature. We used the EDS-fine-tuned weights, which showed gains on higher-motion data in [4]. We qualitatively confirmed the correctness of our modifications on the first 10ms of recordings.

4.4. Benchmark

All three methods were initialized with the same starting positions and scale estimates provided by [7]. In deployment, initialization can be performed by a standard RGB camera, it does not require a high frame rate or low latency. When a tracker fails, *i.e.*, begins to report a wrong RPM, we do not reinitialize. HelixTrack parameters were found by element-wise descent and a grid search around these values (see supplementary Sec. S4). In every fold, the parameters that minimized the training error of HelixTrack were identical, unlike those of AEB-Tracker.

Despite our best-effort adaptations for RPM estimation, the results in Table 1 show that the strongly periodic propeller setting, outside the intended design space of AEB-Tracker and DeepEv, leads to very high failure rates for both methods. The best performance is achieved by HelixTrack. As expected, errors grow with stronger egomotion M_{ego} and with larger capture distance d . Increasing M_{ego} raises the number of background events, further stressing the trackers. In the sequences where HelixTrack fails, we observe abrupt camera movements that coincide with a very low rotation speed (≈ 1352 RPM). Under these conditions,

Event Stride	MAE (RPM) ↓	RTF _{est} ↑	$U_{\text{evt}}/U_{\text{GN}}$
1	105.6±48.8	13.6±3.6	775.00±249.17
2	1382.2±3277.8	30.3±12.5	1520.84±1477.22
3	1339.7±2933.5	42.8±12.2	1081.24±854.28
4	2492.1±3520.2	53.1±22.8	559.09±645.35

Table 2. Runtime-accuracy trade-off for event subsampling. We report mean \pm standard deviation across 4-fold cross-validation on the 23 successfully tracked propellers (MAE ≤ 300 RPM) from Timestamped Quadcopter with Egomotion dataset. Metrics: Mean Absolute Error (MAE, RPM; lower is better), the estimated real-time factor RTF_{est} (higher is better) computed as sequence duration divided by the total compute time (per-event EKF updates plus batched Gauss-Newton (GN) solves), and the mean per-update costs $U_{\text{evt}}/U_{\text{GN}}$ for a single event update and a single GN pose solve, respectively. “Event stride = k ” means only every k -th event is processed. See Sec. 4.5 for the details and definitions.

the phase advance needed to trigger a pose update — half a shaft rotation for a two-blade rotor (*i.e.*, 2π in helical phase) — accumulates too slowly relative to the image-plane motion, so the pose estimate lags and the track can break.

Visualization of HelixTrack tracklets and final projections of per-propeller unit circles is available in Fig. 3, complete results and all parameters in supplementary Sec. S5 and Table S3, and qualitative results in the supplementary video, the C++ implementation in the supplementary codes.

4.5. Runtime Analysis

The *event stride* means processing every k -th event (stride = 1,2,3,4). The RTF_{est} is computed as

$$\text{RTF}_{\text{est}} = \frac{\sum_s \text{duration}_s}{U_{\text{evt}} + U_{\text{GN}}},$$

i.e., the ratio of total sequence time to the sum U_{evt} of all per-event update times and the sum U_{GN} of all GN-solve times (all in μs). We also report $U_{\text{evt}}/U_{\text{GN}}$ exposing the cost profile of the loops. All runtime experiments were executed single-threaded on machines equipped with AMD EPYC 7543 processors. The single-propeller tracker used under 20 MB of memory, including all benchmark storage routines.

The results reported in Table 2 are computed over the 23 successfully tracked propellers (MAE ≤ 300 RPM) from TQE (Sec. 4.1), indicated by \checkmark in supplementary Table S3. Processing all events (stride = 1) achieves RTF_{est} $\approx 13.6 \pm 3.6$ (full dataset RTF_{est} $\approx 11.8 \pm 4.4$), which is comfortably faster than real time, with MAE = 105.6 \pm 48.8 RPM. Subsampling increases throughput, but degrades accuracy.

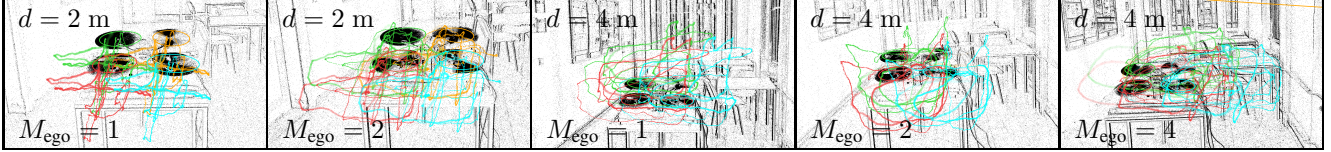


Figure 3. Projection of per-propeller unit circles under the final homography estimate, overlaid with HelixTrack trajectories on selected Timestamped Quadcopter with Egomotion sequences. Propellers are color-coded: rear left green, rear right orange, front left red, front right cyan. Markers encode time: size increases and opacity decreases backward in time, so older states appear larger and more transparent.

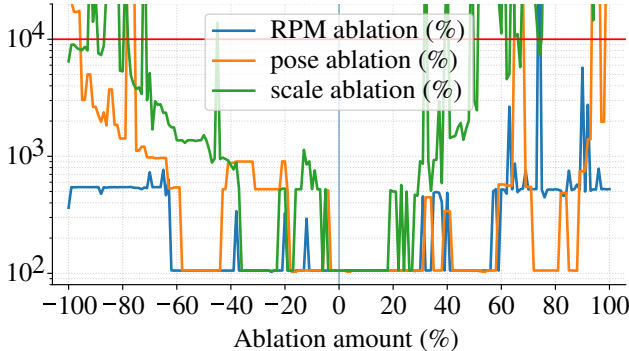


Figure 4. Robustness to initialization errors. We perturb the initial tracker position, in-plane scale, and initial RPM by $\pm\{1, 2, \dots, 100\}\%$ around the nominal initialization and run HelixTrack end-to-end. For position, we average shifts “toward” and “away from” the nearest distractor (propeller). The plot reports shaft-RPM Mean Absolute Error (MAE) across propellers with $\text{MAE} \leq 300$ (lower is better); red line marks 10,000 RPM.

4.6. Initial State Estimate Ablation

Trackers are provided with a coarse initial state (position, radius/scale, weak perspective, and RPM), supplied by the propeller detector [7]. We evaluate how much initialization quality matters by ablating each component independently and measuring the MAE of the estimated shaft RPM across 23 successfully tracked propellers ($\text{MAE} \leq 300$ RPM) from Timestamped Quadcopter with Egomotion (Sec. 4.1), marked with \checkmark in supplementary Table S3. We vary RPM and scale by $\pm\{1, 2, \dots, 100\}\%$ of their nominal values. For position, we translate along the image-plane radial direction by a given fraction of the estimated blade radius and average “toward-distractor” and “away-from-distractor” shifts.

Fig. 4 shows that the system is tolerant to errors in initialization but exhibits sharp, asymmetric failure modes for larger perturbations.

4.7. Loss ablation

A detailed ablation of $(\lambda_\phi, \lambda_r, \lambda_{\text{pol}}, \lambda_{\text{band}}, \lambda_{\text{BTO}})$ terms (4) revealed that the *phase* λ_ϕ and *radial* λ_r data terms provide the backbone for stable pose/phase coupling. The *band* constraints λ_{band} and *polarity* λ_{pol} alignment significantly boost

robustness under distance and high M_{ego} ; and *BTO* λ_{BTO} offers a small but reliable safety margin against occupancy imbalance. Together, these components are necessary to keep the asynchronous EKF and batched GN updates coherent. See the full results in supplementary Sec. S6.

4.8. Limitations

Initialization. Coarse hub position/scale/RPM is required; small errors are tolerated, but larger perturbations ($> 30\%$) often cause failures (Sec. 4.6).

View and geometry. A single planar homography and a helical phase on a visible annulus are assumed; edge-on/side views (severe foreshortening), strong non-planarity, or heavy occlusion violate this model and degrade tracking.

Scene priors. Known blade count and dominance of rotor events in the ring is assumed. However, the blade count may be estimated during initialization.

Reinitialization. HelixTrack does not perform automatic reinitialization after failure. Although feasible, doing so would obscure the evaluation by mixing tracking accuracy with recovery behavior.

5. Conclusion

We presented HelixTrack, a geometry-aware, event-native tracker that turns the periodicity of a spinning propeller into a modeling advantage. By lifting events to rotor-plane coordinates and enforcing a simple helical phase law, a per-event EKF and batched Gauss-Newton pose updates jointly deliver trajectories and instantaneous RPM from raw events.

Performance of HelixTrack on the proposed TQE benchmark exposed the difficulty of *single-propeller* tracking in the presence of near-identical, co-rotating distractors and egomotion. Representative asynchronous and learned trackers frequently fail or experience order-of-magnitude errors as motion and distance increase (Table 1). At the same time, HelixTrack produces instantaneous angular-speed and RPM estimates at event resolution, *i.e.*, *microsecond-latency* updates, while sustaining $\approx 11.8\times$ real-time throughput on TQE (Table 2), pairing precise timing with practical speed. Pose updates are triggered adaptively whenever the accumulated helical phase exceeds 2π . This defines an event-driven, self-timed pose-estimation latency typically on the order of tens of *ms*.

References

- [1] Gianluca Ciattaglia, Grazia Iadarola, Linda Senigaglia, Ennio Gambi, and Susanna Spinsante. Measuring UAV Propeller RPM with FMCW Radar: Validation with Calibrated Accelerometers. In *IEEE Sensors Applications Symposium (SAS)*, pages 1–6, 2024. 3
- [2] Jakub Kolář, Radim Špetlík, and Jiří Matas. EEPPR: event-based estimation of periodic phenomena rate using correlation in 3D. In *Seventeenth International Conference on Machine Vision (ICMV 2024)*, pages 223–230. SPIE, 2025. 2
- [3] Siqi Li, Zhikuan Zhou, Zhou Xue, Yipeng Li, Shaoyi Du, and Yue Gao. 3D Feature Tracking via Event Camera. In *IEEE/CVF Conference on Computer Vision and Pattern Recognition*, pages 18974–18983, 2024. 1, 2
- [4] Nico Messikommer, Carter Fang, Mathias Gehrig, Giovanni Cioffi, and Davide Scaramuzza. Data-Driven Feature Tracking for Event Cameras With and Without Frames. *IEEE Transactions on Pattern Analysis and Machine Intelligence*, 47(5):3706–3717, 2025. 1, 2, 6, 7
- [5] Anton Mitrokhin, Cornelia Fermüller, Chethan Parameshwara, and Yiannis Aloimonos. Event-Based Moving Object Detection and Tracking. In *2018 IEEE/RSJ International Conference on Intelligent Robots and Systems (IROS)*, pages 1–9, 2018. 3
- [6] Nitin J. Sanket, Deep Singh Chahat, Chethan M. Parameshwara, Cornelia Fermüller, Guido C.H.E. de Croon, and Yiannis Aloimonos. EVPropNet: Detecting Drones By Finding Propellers For Mid-Air Landing And Following. In *Robotics: Science and Systems 2021*, 2021. 3
- [7] Radim Špetlík, Tereza Uhrová, and Jiří Matas. Efficient Real-Time Quadcopter Propeller Detection and Attribute Estimation with High-Resolution Event Camera. In *Image Analysis*, pages 217–230, 2025. 2, 3, 7, 8
- [8] Terrence Stewart, Marc-Antoine Drouin, Guillaume Gagne, and Guy Godin. Drone Virtual Fence Using a Neuromorphic Camera. In *International Conference on Neuromorphic Systems 2021*, pages 1–9, 2021. 3
- [9] Terrence Stewart, Marc-Antoine Drouin, Michel Picard, Frank Billy Djupkep Dizeu, Anthony Orth, and Guillaume Gagné. A Virtual Fence for Drones: Efficiently Detecting Propeller Blades with a DVXplorer Event Camera. In *Proceedings of the International Conference on Neuromorphic Systems 2022*, pages 1–7, 2022. 3
- [10] Hongze Sun, Rui Liu, Wuque Cai, Jun Wang, Yue Wang, Huajin Tang, Yan Cui, Dezhong Yao, and Daqing Guo. Reliable object tracking by multimodal hybrid feature extraction and transformer-based fusion. *Neural Networks*, 178: 106493, 2024. 1, 2
- [11] Matouš Vrba and Martin Saska. Marker-Less Micro Aerial Vehicle Detection and Localization Using Convolutional Neural Networks. *IEEE Robotics and Automation Letters*, 5(2):2459–2466, 2020. 3
- [12] Song Wang, Zhu Wang, Can Li, Xiaojuan Qi, and Hayden Kwok-Hay So. SpikeMOT: Event-Based Multi-Object Tracking With Sparse Motion Features. *IEEE Access*, 13: 214–230, 2025. 1, 2
- [13] Xiao Wang, Shiao Wang, Chuanming Tang, Lin Zhu, Bo Jiang, Yonghong Tian, and Jin Tang. Event Stream-Based Visual Object Tracking: A High-Resolution Benchmark Dataset and A Novel Baseline. In *IEEE/CVF Conference on Computer Vision and Pattern Recognition*, pages 19248–19257, 2024. 2
- [14] Xiao Wang, Chao Wang, Shiao Wang, Xixi Wang, Zhicheng Zhao, Lin Zhu, and Bo Jiang. MambaEVT: Event Stream based Visual Object Tracking using State Space Model. *IEEE Transactions on Circuits and Systems for Video Technology*, 2025. 1, 2
- [15] Ziwei Wang, Timothy Molloy, Pieter van Goor, and Robert Mahony. Asynchronous Blob Tracker for Event Cameras. *IEEE Transactions on Robotics*, 40:4750–4767, 2024. 1, 2, 6
- [16] Maria Zafeiri, Georgios Evangelidis, and Emmanouil Psarakis. Event-ECC: Asynchronous Tracking of Events with Continuous Optimization, 2024. 1, 2, 3
- [17] Xu Zheng, Yexin Liu, Yunfan Lu, Tongyan Hua, Tianbo Pan, Weiming Zhang, Dacheng Tao, and Lin Wang. Deep Learning for Event-based Vision: A Comprehensive Survey and Benchmarks, 2024. 3
- [18] Ye Zheng, Canlun Zheng, Jiahao Shen, Peidong Liu, and Shiyu Zhao. Keypoint-Guided Efficient Pose Estimation and Domain Adaptation for Micro Aerial Vehicles. *IEEE Transactions on Robotics*, 40:2967–2983, 2024. 3

HelixTrack: Event-Based Tracking and RPM Estimation of Propeller-like Objects

Supplementary Material

S1. Full Gauss-Newton System with Jacobians

In this section, we describe the full Gauss-Newton System with Jacobians of the terms mentioned in Sec. 3.

Jacobians for all residuals. Let $\sigma(x) = \frac{1}{1+e^{-x}}$ and adopt $\frac{d}{dx} \text{wrap}_\pi(x) = 1$ a.e. For polarity,

$$\delta_i = \text{wrap}_\pi(\varepsilon_i^\phi - d_{\text{pol}}), \quad \varepsilon_i^{\text{pol}} = c_{\text{pol}} \sin(\frac{1}{2}\delta_i),$$

$$\mathbf{J}_i^{\text{pol}} = c_{\text{pol}} \cdot \frac{1}{2} \cos(\frac{1}{2}\delta_i) \mathbf{J}_i^\phi.$$

For soft band barriers,

$$\varepsilon_i^{\text{in}} = c_b \text{softplus}_\tau(r_{\text{in}} - r_i), \quad \varepsilon_i^{\text{out}} = c_b \text{softplus}_\tau(r_i - r_{\text{out}}),$$

$$\mathbf{J}_i^{\text{in}} = -c_b \sigma\left(\frac{r_{\text{in}} - r_i}{\tau}\right) \mathbf{J}_i^r, \quad \mathbf{J}_i^{\text{out}} = c_b \sigma\left(\frac{r_i - r_{\text{out}}}{\tau}\right) \mathbf{J}_i^r.$$

Balanced Tip Occupancy (BTO). Define soft occupancies with temperature τ_{occ} ,

$$m_i^{\text{in}} = \sigma\left(\frac{r_{\text{in}} - r_i}{\tau_{\text{occ}}}\right), \quad m_i^{\text{out}} = \sigma\left(\frac{r_i - r_{\text{out}}}{\tau_{\text{occ}}}\right),$$

$$p_{\text{in}} = \frac{1}{|\mathcal{B}|} \sum_i m_i^{\text{in}}, \quad p_{\text{out}} = \frac{1}{|\mathcal{B}|} \sum_i m_i^{\text{out}}.$$

Then

$$\frac{\partial p_{\text{in}}}{\partial \mathbf{q}} = \frac{1}{|\mathcal{B}|} \sum_i \left[-\frac{1}{\tau_{\text{occ}}} m_i^{\text{in}} (1 - m_i^{\text{in}}) \mathbf{J}_i^r \right],$$

$$\frac{\partial p_{\text{out}}}{\partial \mathbf{q}} = \frac{1}{|\mathcal{B}|} \sum_i \left[\frac{1}{\tau_{\text{occ}}} m_i^{\text{out}} (1 - m_i^{\text{out}}) \mathbf{J}_i^r \right].$$

Let

$$\phi(s) = \text{softplus}_\tau(s), \quad \phi'(s) = \sigma(s/\tau),$$

$$\phi''(s) = \sigma(s/\tau)(1 - \sigma(s/\tau))/\tau$$

and

$$s_{\text{in}}^{\text{lo}} = \underline{p}_{\text{in}} - p_{\text{in}}, \quad s_{\text{in}}^{\text{hi}} = p_{\text{in}} - \overline{p}_{\text{in}},$$

$$s_{\text{out}}^{\text{lo}} = \underline{p}_{\text{out}} - p_{\text{out}}, \quad s_{\text{out}}^{\text{hi}} = p_{\text{out}} - \overline{p}_{\text{out}}.$$

Hence

$$\mathbf{J}_{s_{\text{in}}^{\text{lo}}} = -\frac{\partial p_{\text{in}}}{\partial \mathbf{q}}, \quad \mathbf{J}_{s_{\text{in}}^{\text{hi}}} = \frac{\partial p_{\text{in}}}{\partial \mathbf{q}}, \quad \mathbf{J}_{s_{\text{out}}^{\text{lo}}} = -\frac{\partial p_{\text{out}}}{\partial \mathbf{q}}, \quad \mathbf{J}_{s_{\text{out}}^{\text{hi}}} = \frac{\partial p_{\text{out}}}{\partial \mathbf{q}}.$$

Complete GN system. With frozen gates $g_i^\phi = \lambda_\phi w_i^\phi$ and $g_i^r = \lambda_r w_i^r$,

$$\mathbf{H}_{\text{GN}} = \sum_i g_i^\phi (\mathbf{J}_i^\phi)^\top \mathbf{J}_i^\phi + \sum_i g_i^r (\mathbf{J}_i^r)^\top \mathbf{J}_i^r \quad (\text{S1})$$

$$+ \lambda_{\text{pol}} \sum_i (\mathbf{J}_i^{\text{pol}})^\top \mathbf{J}_i^{\text{pol}} \quad (\text{S2})$$

$$+ \lambda_{\text{band}} \sum_i \left[(\mathbf{J}_i^{\text{in}})^\top \mathbf{J}_i^{\text{in}} + (\mathbf{J}_i^{\text{out}})^\top \mathbf{J}_i^{\text{out}} \right] \quad (\text{S3})$$

$$+ \lambda_{\text{BTO}} \sum_{q \in \{\text{in}, \text{out}\}} \left[\phi''(s_q^{\text{lo}}) (\mathbf{J}_{s_q^{\text{lo}}})^\top \mathbf{J}_{s_q^{\text{lo}}} \right] \quad (\text{S4})$$

$$+ \phi''(s_q^{\text{hi}}) (\mathbf{J}_{s_q^{\text{hi}}})^\top \mathbf{J}_{s_q^{\text{hi}}} \quad (\text{S5})$$

$$+ \mathbf{H}_{\text{reg}}, \quad (\text{S6})$$

$$\mathbf{g} = \sum_i g_i^\phi \varepsilon_i^\phi (\mathbf{J}_i^\phi)^\top + \sum_i g_i^r \varepsilon_i^r (\mathbf{J}_i^r)^\top \quad (\text{S7})$$

$$+ \lambda_{\text{pol}} \sum_i \varepsilon_i^{\text{pol}} (\mathbf{J}_i^{\text{pol}})^\top \quad (\text{S8})$$

$$+ \lambda_{\text{band}} \sum_i \left[\varepsilon_i^{\text{in}} (\mathbf{J}_i^{\text{in}})^\top + \varepsilon_i^{\text{out}} (\mathbf{J}_i^{\text{out}})^\top \right] \quad (\text{S9})$$

$$+ \lambda_{\text{BTO}} \sum_{q \in \{\text{in}, \text{out}\}} \left[\phi'(s_q^{\text{lo}}) (\mathbf{J}_{s_q^{\text{lo}}})^\top + \phi'(s_q^{\text{hi}}) (\mathbf{J}_{s_q^{\text{hi}}})^\top \right] \quad (\text{S10})$$

$$+ \mathbf{g}_{\text{reg}}. \quad (\text{S11})$$

S2. Dataset Details

This section gives a detailed overview of Timestamped Quadcopter with Egomotion dataset.

The average number of ground-truth timestamps is 4 770, maximum 5 116, minimum 4 906, and median is 4 876.

The average number of processed events is 1.7×10^9 , maximum 3.1×10^9 , minimum 1.0×10^9 , and median is 1.6×10^9 .

The average event rate is 60, 4×10^6 (events / second).

In Fig. S1, the aggregated events of the first 10 ms of five 1-second intervals are displayed for all recordings taken at a camera-to-quadcopter distance of 2 m. The intensity of egomotion begins at the top with $M_{\text{ego}} = 1$ and progresses to the last row with $M_{\text{ego}} = 7$. Fig. S2 is structured in the same way and presents recordings for a camera-to-quadcopter distance of 4 m.



Figure S1. Aggregated events from all sequences in the Timestamped Quadcopter with Egomotion dataset with camera-to-quadcopter distance of 2 m, from the smallest (top row, $M_{\text{ego}}=1$), to the largest (bottom row, $M_{\text{ego}}=7$) egomotion intensity. Events from the first 10 ms of five 1-second intervals are shown. Positive events displayed in black, negative in gray.

S3. AEB-Tracker Parameters Grid Search

As described in Sec. 4.3.1, we first tuned the hyperparameters of the tracker qualitatively. Once a well-performing set of parameters was found on the first 10 milliseconds of the recording, we run the grid search described below.

We performed a comprehensive grid search over four AEB-tracker hyperparameters, 72 combinations in total, evaluated across all recordings and channels. The parameters are as follows.

1. rb (ring_buffer_len): Length of the per-target event/state ring buffers. Larger values smooth estimates more but add inertia,
2. Δt : Integration timestep (seconds) used in the state transition F for (x, y, θ) ; in particular $\theta \leftarrow \theta + q dt$,
3. q_{xy} : Sets both velocity process-noise intensities q_{v_x} and

q_{v_y} [px^2/s^3]. Larger values allow faster changes in velocity (more agility) at the cost of more noise/jitter.

4. q_q : Sets the spin-rate process-noise intensity q_q [rad^2/s^3]. Larger values let the angular velocity q vary more between updates.

We select the setting that minimizes mean absolute error (MAE). We also report std/median and mean absolute relative error (MArE).

The best configuration observed in Table S4 is $rb = 22$, $\Delta t = 2.5$, $q_{xy} = 5.0$, $q_q = 0.5$, achieving MArE 502.976 and MAE of 38763.807 (aggregated over all recordings and channels).



Figure S2. Aggregated events from all sequences in the Timestamped Quadcopter with Egomotion dataset with camera-to-quadcopter distance of 4 m, from the smallest (top row, $M_{\text{ego}}=1$), to the largest (bottom row, $M_{\text{ego}}=7$) egomotion intensity. Events from the first 10 ms of five 1-second intervals are shown. Positive events displayed in black, negative in gray.

S4. HelixTrack Parameter and Grid Search

We set the parameters of HelixTrack with a combination of element-wise search and grid search. The complete set of parameters we searched for and their final values are: $q_{\text{jerk}} = 400$, $\lambda_{\phi} = 1.0$, $\lambda_r = 1.0$, $\lambda_{\text{pol}} = 0.25$, $\lambda_{\text{band}} = 5.0$, $\lambda_{\text{BTO}} = 1.0$, $r_{\text{in}} = 0.2$, $r_{\text{out}} = 1.5$, $\gamma_{\text{tx}} = \gamma_{\text{ty}} = 6.0$, $\gamma_{\text{persp}} = 1.0$. For the complete set of all parameters, not just the ones we searched for, see the attached configuration file and codes.

The grid search was performed over r_{in} and r_{out} parameters, results are in Table S1.

The element-wise search was performed with the following set of parameters:

- q_{jerk} (7): 50, 100, 200, 300, 400, 500, 600
- λ_{ϕ} (2): 0, 1
- λ_r (2): 0, 1
- λ_{pol} (6): 0, 0.25, 0.5, 1, 2, 10
- λ_{band} (5): 0, 1, 5, 10, 20
- λ_{tip} (5): 0, 0.5, 1, 2, 10
- $\gamma_x = \gamma_y$ (7): 1, 2, 3, 4, 5, 6, 7

- γ_{persp} (5): 0.01, 0.1, 1, 2, 3

In total, **275** unique experiment configurations were examined, not including the grid search for r_{in} and r_{out} .

S5. Benchmark Complete Results

Across all cells of the Table S3, HelixTrack is consistently the most accurate. It achieves the lowest error in 43/52 (MArE), 46/52 (MAE), and 45/52 (RMSE) cases, while AEB-Tracker wins 8/6/5 and DeepEv 1/0/2, respectively. When we compute medians to mitigate heavy-tailed failures, HelixTrack reduces error dramatically relative to AEB-Tracker — MArE: 400.05 \rightarrow 58.95 (-85.3%), MAE: 29,859.50 \rightarrow 5,200.3 (-82.6%), RMSE: 51,662.7 \rightarrow 6,332.25 (-87.7%). DeepEv’s medians for MAE/RMSE (14,459.0 / 19,504.4) are below the medians of AEB-Tracker, but its means are much higher due to frequent catastrophic failures.

Effect of distance d . Performance improves with increased camera-scene distance for HelixTrack. At $d = 2\text{m}$ vs. 4m , HelixTrack’s medians drop from 63.65 \rightarrow 29.65 (MArE),

r_{in}	r_{out}	MAE (RPM) ↓	median
0.0	1.4	25897.838 ± 64560.838	6837.504
0.0	1.5	31173.431 ± 89359.956	6623.163
0.0	1.6	21958.240 ± 62330.271	7017.397
0.0	1.7	33919.799 ± 133795.000	7763.656
0.0	1.8	17984.723 ± 43510.488	6545.428
0.0	1.9	15783.097 ± 43241.885	7078.281
0.1	1.4	4356.810 ± 3985.889	4434.631
0.1	1.5	4814.578 ± 5064.586	4995.041
0.1	1.6	4775.841 ± 3918.283	6323.458
0.1	1.7	4951.189 ± 4428.663	5219.091
0.1	1.8	4687.726 ± 4220.879	5265.247
0.1	1.9	10199.062 ± 39763.741	5339.970
0.2	1.4	10659.736 ± 44302.860	5516.170
0.2	1.5	4052.139 ± 3779.222	5200.247
0.2	1.6	4626.934 ± 3815.512	6050.976
0.2	1.7	4574.203 ± 4136.607	5391.578
0.2	1.8	4691.997 ± 4598.824	5790.502
0.2	1.9	4500.675 ± 3892.523	5436.960
0.3	1.4	6470.363 ± 12126.974	6095.369
0.3	1.5	4401.135 ± 3951.049	5629.956
0.3	1.6	43303.116 ± 274072.299	5758.449
0.3	1.7	4846.586 ± 5777.108	5273.668
0.3	1.8	5826.368 ± 8064.029	5181.593
0.3	1.9	29329.222 ± 179744.825	5588.616

Table S1. Grid search over r_{in} and r_{out} with $q_{jerk}=400$, $\lambda_\phi=1.0$, $\lambda_r=1.0$, $\lambda_{pol}=0.25$, $\lambda_{band}=5.0$, $\lambda_{BTO}=1.0$, $\gamma_x=\gamma_y=6.0$, $\gamma_{persp}=1.0$. The best setting (lowest MAE mean) is highlighted in bold. See Sec. S4

5,233.10 → 2,697.55 (MAE), and 6,461.30→3,358.60 (RMSE). Compared to AEB-Tracker, the improvement widens at longer distance: $d = 2m$: -84.1% / 82.5% / 87.5% (MAE/MAE/RMSE); $d = 4m$: -94.9% / 94.0% / 95.5%. A plausible explanation is that the propeller occupies a smaller angular extent and generates fewer disruptive events at larger d , which HelixTrack exploits more effectively than the baselines.

Effect of ego-motion magnitude M_{ego} . As motion increases, all methods degrade, but HelixTrack degrades more gracefully. For MAE (medians), HelixTrack stays low for $M_{ego} = 1 - 3$, and rises for $M_{ego} = 4 - 7$ — still well below the results of AEB-Tracker. AEB-Tracker shows a pronounced failure at moderate-to-high motion (also reflected in RMSE), while DeepEv exhibits a non-monotonic pattern with moderate medians at certain bins but very heavy tails overall.

Sensitivity to propeller position. The position of a propeller with respect to other propellers / distractors, matters., HelixTrack’s easiest configuration is front-left. The

most challenging is rear-right, followed by front-right and rear-left. Despite this, HelixTrack still secures the majority of wins in every placement: for example, in front-left it wins 13/13 cells for each metric, and even in rear-right it wins 12/13 (MAE/RMSE) and 11/13 (MAE).

AEB-Tracker collects isolated wins (e.g., low motion with favorable geometry), and DeepEv takes two RMSE cells in specific configurations. However, these wins are not robust: the corresponding 95th percentiles and maxima reveal frequent large errors and outright failures, especially for DeepEv. In contrast, HelixTrack shows low variance in most of the grid.

S6. Loss ablation

The results of the loss term ablation in Table S2 show that removing either the phase-geometry coupling ($\lambda_\phi = 0$) or the radial centering term ($\lambda_r = 0$) leads to failure or order-of-magnitude error increases. For example, at 2 m, $M_{ego} = 2$, MAE jumps from 90.1 ± 16.9 (full loss) to 9327.1 ± 175.7 when $\lambda_r = 0$; at 4 m, $M_{ego} = 3$ it rises from 3449.3 ± 3961.3 to 9775.1 ± 129.5 when $\lambda_r = 0$. Tying the Gauss-Newton pose update to phase residuals r_ϕ and keeping events centered on the blade ring via r_r are important for stabilizing geometry and phase jointly (Sec. 3.5, Eq. 4).

Disabling the soft band-edge barriers ($\lambda_{band} = 0$) frequently causes failures in the harder settings (average column reports failure; e.g., 2 m, $M_{ego} = 4$ and 2 m, $M_{ego} = 7$ both fail), indicating that the annulus constraints are necessary to keep the optimization from leaking inside/outside the informative blade band when background motion and perspective effects are large.

Dropping the polarity term ($\lambda_{pol} = 0$) degrades the overall average from 4052.1 ± 2135.0 to 7070.4 ± 3146.3 and can sharply increase error in challenging cases (e.g., 4 m, $M_{ego} = 4$: 2152.1 ± 4126.9 to 8055.4 ± 1451.6), suggesting that softly aligning polarity clusters with the expected blade edge improves robustness.

Removing BTO ($\lambda_{BTO} = 0$) changes the overall average modestly. This is consistent with BTO’s role in discouraging degenerate “only-inside/only-outside” fits rather than driving the solution on its own.

Overall, the *phase* and *radial* data terms provide the backbone for stable pose/phase coupling. The *band* constraints and *polarity* alignment significantly boost robustness under distance and high M_{ego} ; and *BTO* offers a small but reliable safety margin against occupancy imbalance. Together, these components are necessary to keep the asynchronous EKF and batched GN updates coherent.

d	M_{ego}	all	$\lambda_\phi = 0$	$\lambda_r = 0$	$\lambda_{\text{pol}} = 0$	$\lambda_{\text{band}} = 0$	$\lambda_{\text{BTO}} = 0$
2 m	1	92.8 ± 18.4	98.8 ± 21.5	F	5701.9 ± 3786.9	92.8 ± 18.4	92.8 ± 18.4
2 m	2	90.1 ± 16.9	2347.5 ± 2766.6	9327.1 ± 175.7	2103.3 ± 4024.6	89.7 ± 16.6	90.1 ± 16.9
2 m	3	680.2 ± 974.9	3883.1 ± 7372.4	8430.9 ± 1589.7	7438.6 ± 1700.5	1319.7 ± 1522.6	612.5 ± 841.1
2 m	4	7212.5 ± 332.2	7807.8 ± 3357.2	8720.0 ± 1068.0	7427.7 ± 950.7	F	6821.1 ± 475.0
2 m	5	7488.4 ± 2162.5	6718.4 ± 2246.1	F	7142.7 ± 1866.7	7452.8 ± 1056.6	8434.2 ± 974.4
2 m	6	7981.4 ± 1705.1	8902.2 ± 307.7	8210.8 ± 2099.4	8182.7 ± 1695.0	7997.8 ± 1939.9	7868.9 ± 899.4
2 m	7	6497.4 ± 1534.1	F	9194.3 ± 240.5	7873.5 ± 1519.3	F	8032.8 ± 573.4
4 m	1	1721.3 ± 3263.3	2176.4 ± 4171.0	9056.5 ± 197.7	F	1783.8 ± 3388.9	2078.1 ± 3976.9
4 m	2	2210.3 ± 4234.0	2319.0 ± 4439.3	9144.2 ± 202.0	4762.0 ± 4837.7	2263.6 ± 4340.8	1926.3 ± 3666.0
4 m	3	3449.3 ± 3961.3	4670.2 ± 3608.3	9775.1 ± 129.5	5903.4 ± 4194.7	4409.7 ± 5026.2	3402.7 ± 3953.5
4 m	4	2152.1 ± 4126.9	4795.1 ± 5431.6	9617.7 ± 224.8	8055.4 ± 1451.6	4582.6 ± 5204.8	2301.9 ± 4426.5
4 m	5	6969.2 ± 4582.9	5955.7 ± 3973.0	9573.0 ± 229.7	8630.4 ± 2381.1	6913.1 ± 4549.0	6705.8 ± 4456.2
4 m	6	6132.8 ± 842.3	8208.1 ± 1158.6	F	7688.5 ± 623.2	6251.3 ± 2277.5	7990.8 ± 1147.7
Average		4052.1 ± 2135.0	F	F	7070.4 ± 3146.3	F	4335.2 ± 1955.8

Table S2. Loss term ablation. Mean Absolute Error (MAE) of RPM (lower is better) under 4-fold cross-validation on the *Timestamped Quadcopter with Egomotion* (TQE) dataset, reported for two camera–target distances (2 m / 4 m) and seven egomotion levels M_{ego} . “All” uses the full batch objective in Eq. (4) with: phase–geometry alignment r_ϕ , radial centering r_r , polarity alignment r_{pol} , soft annulus barriers $r_{\text{in}}, r_{\text{out}}$, and Balanced Tip Occupancy ℓ_{BTO} . Each ablation zeroes the indicated coefficient ($\lambda_\phi, \lambda_r, \lambda_{\text{pol}}, \lambda_{\text{band}}, \lambda_{\text{BTO}}$). TQE ground-truth RPM has $\mu \pm \sigma = 11193.5 \pm 3540.2$. Values are mean \pm std.

d	M_{ego}	propeller	MArE (%) ↓			MAE (RPM) ↓			RMSE (RPM) ↓		
			ours	AEB [15]	DeepEv [4]	ours	AEB [15]	DeepEv [4]	ours	AEB [15]	DeepEv [4]
2 m	1	rear right	1.3	61.4	8564.8	93.7 ✓	5980.8	652423.7	215.9	7186.8	785896.2
		rear left	1.3	0.9	402.4	81.4 ✓	73.0	32090.3	241.4	241.2	46466.0
		front left	1.5	35.3	4132.0	118.4 ✓	2487.0	303141.3	194.1	3302.9	359054.3
		front right	1.2	65.5	94.6	77.8 ✓	5650.8	8759.2	186.3	7673.3	9700.4
	2	rear right	1.2	52.1	9523.5	85.0 ✓	4637.6	749060.3	178.9	5549.9	904654.7
		rear left	1.3	1.2	4811.7	87.0 ✓	112.9	357676.3	277.2	457.4	455119.6
		front left	1.5	49.8	478.5	114.0 ✓	3075.8	28118.0	223.5	3879.2	68394.5
		front right	1.1	34.5	7458.3	74.3 ✓	2035.8	562988.0	160.9	3367.3	787219.5
	3	rear right	1.2	1198.7	5013.6	85.1 ✓	102482.5	386360.6	223.2	192935.8	437954.9
		rear left	31.7	15.0	2059.8	2137.8 ×	1696.4	151319.8	4518.8	3482.9	184206.2
		front left	4.2	467.5	5236.2	230.2 ✓	37691.4	376231.1	763.8	81016.3	448776.7
		front right	4.8	1347.9	195.7	267.9 ✓	110056.2	14595.8	1031.9	202948.8	18910.5
4	rear right	80.2	1241.2	12474.4	7634.3 ×	93995.4	934583.8	9184.5	182884.8	1141131.4	
	rear left	72.2	24.5	8678.3	7135.2 ×	2828.9	674615.2	8699.8	4782.1	824811.5	
	front left	79.3	410.3	89.2	7249.8 ×	29227.1	8417.0	8825.0	68684.3	9362.8	
	front right	76.3	59.5	115.2	6830.5 ×	5933.1	9027.6	8459.0	11580.7	10408.5	
5	rear right	62.3	531.3	106.7	6347.2 ×	41415.3	9244.0	7842.7	79321.0	10241.1	
	rear left	100.9	480.0	117.9	9689.7 ×	30491.9	10624.2	10899.5	67097.7	12239.0	
	front left	65.0	389.8	99.3	5045.3 ×	33458.3	8963.0	6266.7	69659.2	9836.3	
	front right	97.7	1122.0	398.5	8871.4 ×	77151.0	32523.2	9710.6	111267.4	56823.0	
6	rear right	93.6	726.2	98.1	8928.2 ×	56816.8	9461.9	9874.9	72370.2	10223.4	
	rear left	97.2	593.1	108.1	9221.9 ×	41752.5	9932.7	10100.1	56316.4	11232.3	
	front left	89.5	885.2	103.3	8283.4 ×	61735.0	9163.9	9331.8	72061.8	10279.6	
	front right	57.2	833.4	96.8	5492.3 ×	58682.1	8881.7	6655.9	72261.9	9697.5	
7	rear right	72.2	609.8	10417.8	7194.7 ×	44713.1	780191.6	8292.1	51904.1	894151.1	
	rear left	119.1	617.6	97.0	8328.7 ×	45454.3	9180.8	10071.3	51421.3	10022.4	
	front left	75.7	218.3	96.4	5341.7 ×	16859.6	8811.8	6817.1	28904.6	9686.0	
	front right	72.2	248.4	3638.0	5124.5 ×	17502.1	253240.6	6262.9	29616.6	315329.1	
4 m	1	rear right	73.1	285.5	834.5	6616.3 ×	21029.7	57801.3	8517.8	46759.1	73901.3
		rear left	1.2	57.2	89.6	76.4 ✓	6038.7	8341.9	158.4	20115.0	9422.8
		front left	1.4	48.9	88.7	104.8 ✓	4676.4	7853.7	255.3	16769.4	8925.9
		front right	1.3	165.4	835.4	87.8 ✓	13041.8	58054.3	319.4	36853.1	74833.5
	2	rear right	91.1	43.1	93.1	8561.2 ×	3847.8	8671.9	9537.1	4496.9	9642.0
		rear left	1.3	37.4	3242.1	85.7 ✓	3529.9	241975.2	273.2	5020.2	334534.1
		front left	1.5	72.1	93.8	112.9 ✓	6545.9	8536.3	254.1	17753.2	9595.1
		front right	1.3	77.3	111.7	81.4 ✓	4335.3	8969.8	248.9	17551.4	10429.0
	3	rear right	70.9	58.8	95.8	5770.0 ×	5904.9	9773.3	7008.1	11479.0	10725.7
		rear left	1.3	46.8	1801.4	85.0 ✓	3960.0	140787.4	211.7	4845.4	181653.8
		front left	1.3	303.1	1937.2	109.4 ✓	21349.0	146814.9	210.8	51357.9	174482.0
		front right	79.8	39.7	97.4	7832.8 ×	4091.3	9594.5	9394.6	5306.3	10465.4
4	rear right	83.5	1194.9	95.2	8342.3 ×	101987.0	9517.6	9491.6	201102.2	10384.6	
	rear left	1.1	915.1	5251.8	77.6 ✓	76275.0	426131.2	222.5	179370.3	537350.6	
	front left	1.4	1392.2	389.6	111.6 ✓	98307.7	26933.9	288.4	201185.3	46853.8	
	front right	1.2	1166.3	13.3	76.9 ✓	86077.0	693.4	209.4	191384.9	2370.2	
5	rear right	95.3	994.6	97.8	9688.6 ×	83816.5	9942.3	10614.2	127547.1	10817.5	
	rear left	93.9	1043.3	94.8	9316.3 ×	76882.9	9332.0	10400.6	133235.2	10351.1	
	front left	1.7	1092.8	3339.1	119.1 ✓	81598.8	260136.5	241.1	126119.1	310936.4	
	front right	88.3	1126.9	95.6	8752.7 ×	93336.6	9351.7	9711.9	134050.9	10281.2	
6	rear right	62.1	862.2	167.5	6778.5 ×	68419.4	14322.1	8015.9	97991.7	20098.2	
	rear left	57.6	958.9	3772.0	5547.2 ×	71680.8	290173.7	6746.4	101283.8	359570.3	
	front left	71.5	995.9	11718.5	6929.4 ×	76394.7	918479.2	8522.6	105034.9	1024071.7	
	front right	60.3	856.0	130.4	5276.0 ×	68594.4	12657.2	6397.8	102062.7	18155.9	

Table S3. Benchmark, Timestamped Quadcopter with Egomotion (TQE). For each presented method and setting (camera-target distance d , egomotion level M_{ego}), the average shaft-RPM mean absolute relative error (MArE), mean absolute error (MAE), and root mean squared error (RMSE) are reported over 4-fold cross-validation across the four propellers (one training propeller per fold). Both AEB-Tracker [15] and DeepEv [4] methods were modified to allow RPM estimation (see Sec. 4.3). TQE ground-truth RPM has $\mu \pm \sigma = 11193 \pm 3540$, min 917, max 15768. $M_{\text{ego}} = 1$ roughly means “slow camera movement”, while $M_{\text{ego}} = 5$ means “fast camera movement” (see Fig. 2). As M_{ego} increases, the camera experiences stronger egomotion, leading to increase of the number of events generated in the background.

rb	Δt	q_{xy}	q_q	MArE (%)	↓	median	MAE (RPM)	↓	median
22	2	0.2	0.25	496.419 ± 402.402		428.662	39026.775 ± 35704.452		27149.123
22	2	0.2	0.5	538.978 ± 532.238		335.813	41383.706 ± 40575.234		24252.682
22	2	0.2	1	650.760 ± 610.255		580.914	49669.433 ± 45197.183		44281.303
22	2	0.2	2	697.412 ± 668.144		537.904	53110.765 ± 50873.870		39796.295
22	2	1	0.25	587.555 ± 478.454		411.100	39086.051 ± 29527.280		26570.284
22	2	1	0.5	544.618 ± 510.582		401.498	41860.949 ± 39341.854		30303.074
22	2	1	1	615.645 ± 577.918		553.496	47675.376 ± 44307.127		42378.293
22	2	1	2	694.885 ± 662.955		577.022	52290.860 ± 49815.795		42225.829
22	2	5	0.25	510.618 ± 388.804		397.497	39608.748 ± 29903.648		29931.931
22	2	5	0.5	506.789 ± 472.468		400.054	38952.001 ± 36484.847		29859.506
22	2	5	1	637.420 ± 590.571		597.896	48856.215 ± 44965.901		44515.639
22	2	5	2	664.801 ± 623.023		618.496	50721.102 ± 47445.002		46145.155
22	2.5	0.2	0.25	599.204 ± 405.217		428.662	39154.585 ± 31844.812		27149.123
22	2.5	0.2	0.5	541.204 ± 535.575		335.813	41498.917 ± 40751.855		24252.682
22	2.5	0.2	1	656.356 ± 608.960		626.036	50086.419 ± 45131.954		46723.292
22	2.5	0.2	2	700.457 ± 672.777		537.904	53245.557 ± 51105.783		39796.295
22	2.5	1	0.25	582.944 ± 578.059		404.861	39748.436 ± 29535.466		26218.892
22	2.5	1	0.5	546.194 ± 513.463		401.498	41776.215 ± 39284.539		30303.074
22	2.5	1	1	619.680 ± 584.761		553.496	48030.629 ± 44997.063		42378.293
22	2.5	1	2	696.192 ± 666.004		577.022	52501.734 ± 50255.610		42225.829
22	2.5	5	0.25	511.004 ± 391.626		362.751	39689.789 ± 30294.397		29321.017
22	2.5	5	0.5	502.976 ± 462.531		400.054	38763.807 ± 35860.448		29859.506
22	2.5	5	1	635.099 ± 588.028		597.896	48705.017 ± 44782.988		44515.639
22	2.5	5	2	667.087 ± 627.251		618.496	50801.457 ± 47640.824		46145.155
22	3	0.2	0.25	537.926 ± 339.939		388.690	40797.556 ± 25179.970		32766.673
22	3	0.2	0.5	527.948 ± 330.960		482.435	39522.724 ± 23976.905		36248.414
22	3	0.2	1	1572.458 ± 1439.686		1071.014	118593.768 ± 108749.883		77281.079
22	3	0.2	2	1729.390 ± 1080.637		1360.253	130145.474 ± 80259.290		110851.655
22	3	1	0.25	510.972 ± 337.896		387.988	39089.727 ± 25213.444		29948.624
22	3	1	0.5	522.499 ± 311.308		439.585	39133.979 ± 22301.822		32878.498
22	3	1	1	1623.040 ± 1543.883		999.876	122206.230 ± 115777.126		76014.113
22	3	1	2	1819.391 ± 1076.640		1690.690	137646.186 ± 80980.053		131528.893
22	3	5	0.25	528.778 ± 327.504		393.982	39501.077 ± 24184.137		30356.179
22	3	5	0.5	620.653 ± 478.684		477.139	46596.672 ± 35946.071		36226.416
22	3	5	1	1775.582 ± 1666.385		1223.899	133680.214 ± 125213.233		87960.026
22	3	5	2	1868.451 ± 1043.308		1612.597	140173.319 ± 78815.962		128391.421
33	2	0.2	0.25	532.076 ± 542.658		313.137	40817.897 ± 42290.509		23969.480
33	2	0.2	0.5	637.817 ± 621.567		359.301	49911.826 ± 48999.356		28496.135
33	2	0.2	1	722.345 ± 689.412		658.855	54920.949 ± 53254.591		47154.050
33	2	0.2	2	801.631 ± 764.621		785.360	61030.529 ± 59447.827		53700.933
33	2	1	0.25	539.595 ± 519.382		358.879	41270.586 ± 40010.637		28240.227
33	2	1	0.5	628.204 ± 611.694		431.265	48692.147 ± 47599.814		29409.219
33	2	1	1	756.455 ± 724.681		638.275	57933.012 ± 56141.403		47235.750
33	2	1	2	764.616 ± 729.480		607.390	58027.384 ± 56269.086		46369.599
33	2	5	0.25	594.884 ± 547.826		405.281	45212.128 ± 41849.225		29930.397
33	2	5	0.5	610.897 ± 618.423		408.550	47681.510 ± 48051.032		30428.694
33	2	5	1	767.419 ± 722.414		736.989	58523.058 ± 55635.939		54296.780
33	2	5	2	730.990 ± 714.165		662.121	55352.472 ± 55168.873		49709.951
33	2.5	0.2	0.25	543.074 ± 522.441		313.137	41890.431 ± 41373.974		24346.624
33	2.5	0.2	0.5	639.535 ± 619.235		401.370	50020.820 ± 48816.418		30022.854
33	2.5	0.2	1	727.481 ± 698.813		668.252	55288.661 ± 54127.417		47256.535
33	2.5	0.2	2	796.948 ± 755.814		785.360	60555.252 ± 58419.579		53700.933
33	2.5	1	0.25	532.410 ± 506.342		358.879	41036.682 ± 39777.801		28240.227
33	2.5	1	0.5	628.658 ± 612.606		431.265	48665.147 ± 47531.149		29409.219
33	2.5	1	1	743.469 ± 715.875		624.827	57122.147 ± 55425.865		45484.744
33	2.5	1	2	768.513 ± 746.872		601.761	58471.489 ± 57907.022		45485.936
33	2.5	5	0.25	580.653 ± 485.517		490.506	44371.759 ± 38134.757		35223.893
33	2.5	5	0.5	611.000 ± 617.790		408.550	47776.018 ± 48238.017		30428.694
33	2.5	5	1	760.575 ± 742.399		681.596	58266.260 ± 57509.586		48980.242
33	2.5	5	2	727.158 ± 722.614		597.588	54981.420 ± 55610.817		46677.389
33	3	0.2	0.25	780.803 ± 691.614		539.572	56835.266 ± 50675.677		40003.480
33	3	0.2	0.5	711.595 ± 534.618		538.977	52049.844 ± 39029.338		41273.869
33	3	0.2	1	1334.438 ± 1139.468		903.428	98922.204 ± 83349.423		68183.272
33	3	0.2	2	1800.403 ± 1083.555		1388.857	133261.705 ± 80987.728		101892.368
33	3	1	0.25	797.649 ± 670.641		528.780	58814.987 ± 49205.799		37539.753
33	3	1	0.5	752.721 ± 578.674		586.153	56295.285 ± 43346.004		42539.879
33	3	1	1	1371.708 ± 1131.488		885.898	100812.434 ± 83139.604		65690.880
33	3	1	2	1882.050 ± 1109.445		1727.309	138601.952 ± 83147.089		128224.109
33	3	5	0.25	705.389 ± 592.629		559.554	52950.606 ± 43547.516		42432.900
33	3	5	0.5	713.524 ± 573.891		534.925	52982.647 ± 42424.617		39459.804
33	3	5	1	1401.862 ± 1125.218		929.897	102499.465 ± 82047.435		64251.491
33	3	5	2	1843.070 ± 1090.486		1565.962	136415.532 ± 80887.240		122453.756

Table S4. AEB-Tracker grid search results. MAE and MArE reported as $\mu \pm \sigma$. See Sec. S3 for description.